Applied Thermal Engineering 113 (2017) 1596–1609

Contents lists available at ScienceDirect

Applied Thermal Engineering

journal homepage: www.elsevier.com/locate/apthermeng

Research Paper

Bubble dynamics of water-ethanol mixture during subcooled flow boiling in a conventional channel

B.G. Suhas *, A. Sathyabhama

Mechanical Engineering Department, National Institute of Technology, Karnataka, Srinivasanagara, Surathkal, Mangalore 575025, India

HIGHLIGHTS

- Bubble dynamic analysis is carried for water ethanol mixture in the subcooled boiling region.
- The bubble departure diameter is measured and its relation with heat transfer coefficient is discussed.
- A new empirical correlation is developed to predict the heat transfer coefficient for water.
- The bubble lift-off and bubble sliding are determined.
- Force balance is carried out to determine the possible mechanisms governing the bubble dynamics.

ARTICLE INFO

Article history:
Received 23 July 2016
Revised 30 September 2016
Accepted 18 November 2016
Available online 19 November 2016

Keywords:
Dimensionless bubble departure diameter
Dimensionless time
Waiting period
Growth period
Lift-off
Sliding

ABSTRACT

In this paper, bubble dynamics in subcooled flow boiling of water-ethanol mixture in horizontal rectangular channels is investigated through visualization. The subcooled flow boiling heat transfer coefficient of water ethanol mixtures are determined for various heat flux, mass flux and ethanol volume fraction. A new empirical correlation is proposed to predict the heat transfer coefficient of pure water based on the parameters like heat flux, bubble departure diameter, waiting period and the growth period. Two types of bubble behaviours are observed after nucleation: (i) Sliding for a distance along the bottom wall of the channel surface before lift-off and (ii) Lift-off from the bottom wall of the channel surface without sliding. Force balance analysis is carried out to determine the reason for bubble lift-off and bubble sliding. The bubble lift-off without sliding is observed at higher ethanol volume fraction, lower heat flux and higher channel inlet temperature. The bubble sliding and lift-off are observed at higher heat flux and lower channel inlet temperature for water and water-ethanol mixture of 25% ethanol volume fraction. However, the effect of mass flux on the bubbles sliding or bubble lift-off is not significant.

© 2016 Elsevier Ltd. All rights reserved.

1. Introduction

The bubble dynamics is qualitative as well as quantitative description of the bubble growth in the flow boiling conditions. The bubble behaviour analysis during subcooled flow boiling is very important in understanding the bubble dynamics and boiling heat transfer [1–5]. Initially, a small bubble lies above the superheated wall which gradually grows in size. The bubble growth is governed by the forces on the bubble-liquid-wall interfaces. This stage is known as inertia controlled stage of the bubble growth. In the later stage, as the bubble grows, it comes in contact with the liquid at subcooled region. The bubble growth for this stage is controlled by the rate of liquid evaporation into the bubble [6].

Bubble behaviour in subcooled flow boiling was studied by many researchers. Gunther [7] observed that bubbles collapsed while sliding along the heated surface of bottom wall of the channel. Basu et al. [8] studied the effect of contact angle during the onset of nucleate boiling (ONB). They found that some of the nucleation sites were not active due to flooding and delay ONB. Bibeau and Salcudean [9] conducted an experiment on subcooled flow boiling of water. They found that the bubbles were sliding along the heated surface of channel before being ejected into the bulk subcooled liquid. Since the bubbles were collapsed due to condensation, they did not travel further after nucleation. Zeitoun and Shoukri [10] observed that the bubbles detached from the channel surface. They developed an empirical correlation for the mean bubble departure diameter as a function of the Reynolds number, Jakob number and the boiling number. Okawa et al. [11] studied the bubble behaviour of water in the subcooled boiling region. They observed that some of the bubbles slid along the vertical sur-

* Corresponding author.
E-mail address: suhas_bg@yahoo.co.in (B.G. Suhas).

http://dx.doi.org/10.1016/j.applthermaleng.2016.11.126
1359-4311/© 2016 Elsevier Ltd. All rights reserved.

Nomenclature

C_p	specific heat (kJ/kg-K)
d	bubble diameter (mm)
d^+	dimensionless bubble diameter during departure
d^*	dimensionless bubble diameter at instant time
Exp	experimental
k	thermal conductivity (kW/m-K)
F_b	buoyancy force (N)
F_{cp}	contact pressure force for the bubble (N)
F_{du}	unsteady drag force on the bubble (N)
F_h	force due to the hydrodynamic pressure (N)
F_{qs}	quasi steady-drag in the flow direction (N)
F_s	surface tension force (N)
F_{sl},	shear lift force (N)
F_x	force parallel to flow direction (N)
F_y	force normal to flow direction (N)
h	heat transfer coefficient (kW/m^2-K)
h_{fg}	latent heat of vapourization (kJ/kg)
Ja	Jakob number
q''	heat flux (kW/m^2)
r	bubble radius (mm)
r^+	dimensionless bubble departure radius
t	time (ms)
t^*	dimensionless growth period
T	temperature (K)
ΔT	temperature difference (K)
X	position (m)

Greek letters

α	thermal diffusivity (m^2/s)
ρ	density (kg/m^3)
μ	dynamic viscosity (kg/m-s)
u_τ	friction velocity
σ_s	surface tension (N/m)
ω	uncertainty
θ	contact angle

Subscript

b	bubble point
cp	calculated parameter
d	dew point
dep	departure
Exp	experimental
f	fluid
fr	first row
fw	wall and fluid
g	growth
i	first sample
i+1	first sample
IN	inlet
ip	independent parameter
l	liquid phase
N	total number of samples
Pred	predicted
sub	subcooled
sr	second row
v	vapour phase
σ	standard deviation
w	waiting
W	wall

face and never lifted-off. But few of them lifted off the surface after sliding along the surface. Thorncroft et al. [12] observed the bubble behaviour in subcooled vertical flow boiling using FC-87. They found that the bubble slid along the heated surface but did not lift off during upward flow. In contrast, in downward flow, bubbles were lifted off from the nucleation site.

In flow boiling, force balance is carried out in both the direction, i.e., flow direction parallel to the heating surface and normal to heating surface. The theoretical bubble departure size can be determined from force balance [13]. During flow boiling, it is assumed that the bubble detaches if the combination of buoyancy and drag force is able to overcome the force due to surface tension. The drag force includes the quasi-steady drag in the bulk liquid flow direction, the unsteady drag due to asymmetric growth of the bubble inclined in the direction of the liquid flow and the shear lift force [14]. Al-Hayes and Winterton [15] and Klausner et al. [16] have developed expressions for surface tension force based on variation of contact angle along the periphery of the bubble. The surface tension alone is unable to prevent the bubble departure. The liquid drag on the bubble due to asymmetrical bubble growth acting in the direction opposite to liquid flow is important in holding the bubble to its nucleation site before departure. The literature review presented in this paper is related to pure component. The bubble dynamics and force balance analysis are not sufficiently available for mixture subcooled boiling.

In the present work, the water-ethanol mixture is used and the application is cooling HEV battery module. The present work is to determine the effect of heat flux, mass flux, ethanol volume fraction and channel inlet temperature on bubble departure radius, growth period and waiting period. Force balance is carried out to determine the reason for bubble lift-off and bubble sliding along the heated surface of the channel.

2. Methodology

2.1. Experimental setup and procedure

The schematic diagram of experimental test set up is shown in Fig. 1. The experimental test set up is a closed loop having a rectangular aluminium block consisting of two rectangular channels, condenser coil dipped in ice water bath, reservoir, preheater and pump having variable flow rate. The aluminium block consisting of two channels of 10 mm (width) × 10 mm (height) × 150 mm

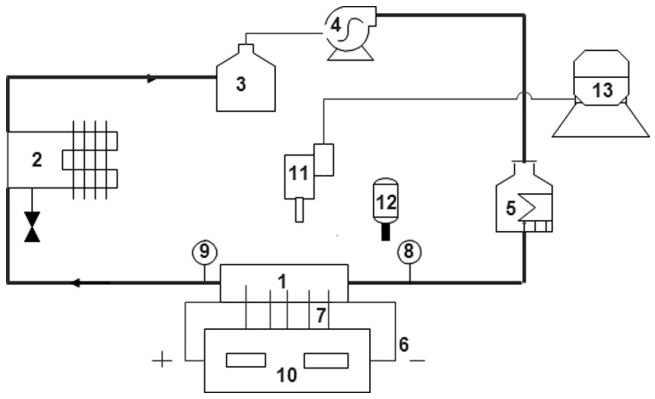

Fig. 1. Schematic diagram of experimental setup. (1) Rectangular aluminium block consisting of two rectangular channels. (2) Condenser coil dipped in ice water bath. (3) Reservoir. (4) Pump having variable flow rate. (5) Preheater. (6) Cartridge heaters. (7) Thermocouples to measure wall temperature. (8) Channel inlet fluid temperature measuring thermocouple. (9) Channel outlet fluid temperature measuring thermocouple. (10) Temperature indicator panel. (11) High speed camera. (12) Light source. (13) Data Acquisition system for flow visualization.

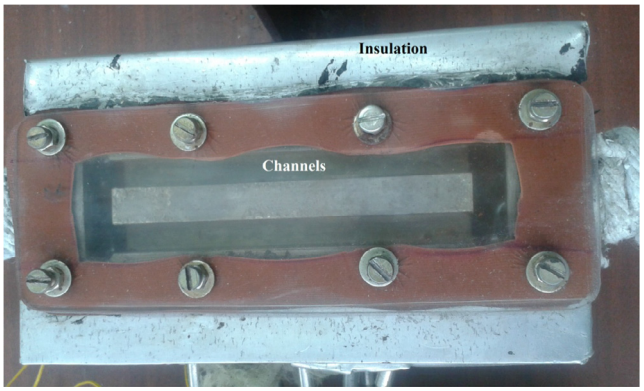

Fig. 2. Aluminium block with rectangular channels.

Table 1
Equipments used in the present experiment.

Equipments	Specifications
k-type thermocouples for wall temperature measurements (10 no's)	Range: −20 °C to 400 °C, sheath length: 20 mm, sheath diameter: 1.2 mm
Cartridge heater (2 no's)	Diameter: 12.7 mm, length: 180 mm, capacity: 750 W
Peristaltic pump	Capacity: 100 L per hour, operating pressure: atmospheric
Preheater	Chamber capacity: 4 L, heater capacity: 3 kW

(Length) is shown in Fig. 2. The two cartridge heaters are inserted inside the aluminium block. Heat loss is prevented by providing mineral wool as insulating material. The wall temperatures, the fluid inlet and outlet temperatures of the channel are measured by thermocouples. The temperature reading is obtained in the temperature indicator panel. The high speed camera is used for flow visualization. Table 1 shows the equipments used in the present experiment. Fig. 3 shows the thermocouples arrangement in the cold plate to measure wall temperature and to calculate heat flux. The first set of five thermocouples (T_{11}, T_{12}, T_{13}, T_{14} and T_{15}) are placed 2 mm below the channel in a row. The second set of five thermocouples (T_{21}, T_{22}, T_{23}, T_{24} and T_{25}) are placed 20 mm below the first row of thermocouples. The distance between each thermocouple in a row is 25 mm. Two cylindrical cartridge heaters are placed 40 mm below the channels.

Due to the possibility of solubility of air in water and ethanol, degassing is done for about thirty minutes before commencing the experiment. The liquid is preheated and pumped through the test set up. The heat is supplied to the channel to boil the liquid. The liquid after getting cooled in the condenser coil enters the reservoir. The experiment is conducted after the degassing procedure.

Table 2
Specifications of high speed camera and source light.

Processor	AOS Promon 501
Lens	50 mm
Aperture setting	f/1.4 D
Shutter speed	1/15
Frames per second	1459
Resolution	480 × 240 pixels
LED PAR light	Slim die cast body, power 120 W, beam 25 degree, CRI > 85, DMX 512 Auto, sound active, 3 section light weight aluminium stand

The steps followed during the experiment are listed below:

1. Fill the water in the reservoir.
2. Set the mass flow rate of the liquid and fix the channel inlet temperature by temperature controller in the preheater.
3. Set a heat input value to the channel such that it must maintain the wall temperature of the channel above the inlet temperature of the liquid.
4. Note down the bottom wall temperature of the channel and outlet temperature of the fluid when the bottom wall temperature of the channel reaches steady state and simultaneously capture the flow by means of high speed camera.
5. Change the volume flow rate and repeat step 4. Increase the volume flow rate so that the laminar flow is maintained.
6. Change the heat input value and repeat step 5. These steps are repeated up to subcooled boiling region (before attaining saturation state).
7. Repeat step 3 to step 6 for two different values of inlet temperatures of the fluid.
8. Repeat step 2 to step 7 for 25%, 50%, 75% and 100% ethanol volume fractions.

Flow visualization is carried out using high speed camera to understand the phenomena of heat transfer during the subcooled flow boiling of the mixture. The LED PAR light is used as light source for proper visibility of the channel. The specifications of high speed camera and LED light are given in Table 2. The camera speed is set for 1459 frames per second and video is recorded for 2 s. The video is converted to images. From the images, the bubble departure diameter and contact angle are measured. The block diagram in Fig. 4 gives the steps which are followed to measure the bubble departure diameter and contact angle by image processing tool in Lab view vision builder software. A tangent is drawn along the bubble as shown in Fig. 5a. The intersection of the tangent and the channel surface is considered as contact angle. The channel width is considered as the Ref. length to measure the departure diameter. The camera is placed at the top of channel and the cam-

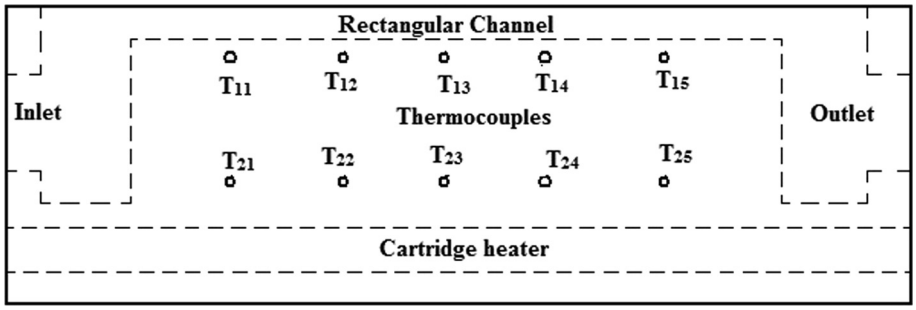

Fig. 3. Thermocouple arrangement in the cold plate.

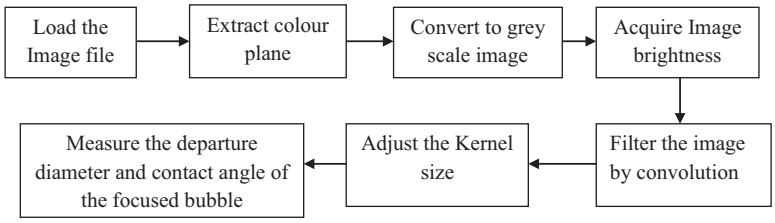

Fig. 4. Image processing.

era is focused as shown in Fig. 5b. Therefore, trigonometric relations are considered to calculate the actual contact angle. However, there is no significant variation in measuring the bubble departure diameters because the bubbles are assumed to be spherical in shape.

From the trigonometric relation:

$$\frac{AB}{BC} = \tan(A^\circ)$$

AB is the distance from the camera lens to the point on the camera stand which is parallel to the bottom wall of channel. BC is the distance from the bottom wall of the channel to the point on the camera stand which is parallel to the bottom wall of channel.

$$A^\circ = \tan^{-1}\left(\frac{AB}{BC}\right)$$

$$\frac{Measured\ \ contact\ \ angle}{Actual\ \ contact\ \ angle} = \frac{AC}{BC} = \frac{AC}{AC\cos(A^\circ)}$$

Actual contact angle = Measured contact angle × cos(A°)

2.2. Data reduction

Bottom wall temperature of the channel is calculated by temperature gradient between the first row and second row of thermocouples in aluminium block. Fourier's law of heat conduction is applied to calculate the heat flux from the measured values of temperature gradient and known value of thermal conductivity.

$$q'' = -k\frac{dT}{dx} \tag{1}$$

The heat flux is calculated by substituting the values of thermal conductivity of aluminium, temperature gradient in Eq. (1) as shown by Eq. (2).

$$q'' = -k\frac{(T_{sr} - T_{fr})}{(X_{sr} - X_{fr})} \tag{2}$$

The heat flux is assumed to be the same for the bottom wall of the channel as the first row, since it is very near to the first rows of thermocouples (i.e. 2 mm). The wall temperature is calculated by Eq. (3).

$$T_W = \frac{-q''}{k}(X_w - X_{fr}) + T_{fr} \tag{3}$$

The heat transfer coefficient is calculated by Eq. (4) from the calculated values of heat flux, calculated values of wall temperature and measured values of outlet temperature. The average of five readings of wall temperature is considered to determine the difference between the wall and fluid temperature. Fluid temperature is the average fluid temperature of the channel inlet and the outlet.

$$h = \frac{q''}{(T_w - T_f)} \tag{4}$$

It is observed that the heat flux value is higher at the inlet of the channel and decreases along length of the channel. It is also observed that the wall temperature is lower at the entrance and marginally increases along the channel length. Therefore the average of five heat fluxes and wall temperatures which are obtained from five different points along the length of the channel are considered to calculate the heat transfer coefficient.

2.3. Uncertainties

According to International Bureau of weights and measures (IBWM) and International organization of standards, (ISO) random independent variables may be calculated using root-sum-square (RSS) of standard deviation [17].

$$\omega_{ip} = \sqrt{\omega_{iresolution}^2 + \omega_{iconversion}^2 + \omega_{icalibration}^2 + s_{2\sigma_i}^2} \tag{5}$$

After determining the uncertainty of independent variables, the uncertainties of calculated parameters are determined by McClintock and Kline method [18].

$$\omega_{cp}^2 = \sum_{i=1}^{n}\left(\frac{\partial f}{\partial x_i}\right)^2 \omega_{x_i}^2 \tag{6}$$

Table 3 shows the uncertainties of independent and measured parameters.

3. Results and discussions

The experiments are conducted to determine the subcooled flow boiling heat transfer coefficient for various values of heat flux (61.33–133.47 kW/m^2), mass flux (76.67–228.33 kg/m^2-s), fluid inlet temperature (303 K, 313 K and 323 K) and ethanol volume fraction (0%, 25%, 50%, 75% and 100%). About 478 experimental runs are carried out in the present study which includes 122 data for pure water, 288 data for three different compositions of binary mixtures, and 68 data for pure ethanol. But the comparison of bubble departure diameter, growth period, waiting period of bubbles in the mixture is carried out at heat flux = 90.4 kW/m^2. This particular value of heat flux is chosen in such a way that the subcooled boiling takes place for both water and ethanol. If the heat flux is lower than 90.4 kW/m^2, subcooled boiling of water will not commence, instead it will be in forced convective region. If the heat flux is higher than 90.4 kW/m^2, saturated boiling of ethanol will be initiated.

3.1. Validation of experimental data of heat transfer coefficient

The experimental values of heat transfer coefficient obtained for water are compared with available subcooled boiling literature correlations. Chen redeveloped the Rohsenow correlation for subcooled boiling heat transfer coefficient [19]:

$$h_{tp} = Fh_{fc} + Sh_{pb} \tag{7}$$

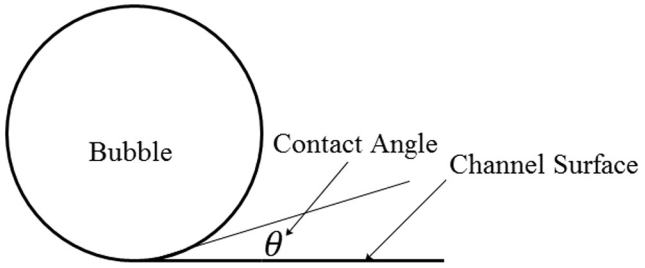

Fig. 5a. Contact angle.

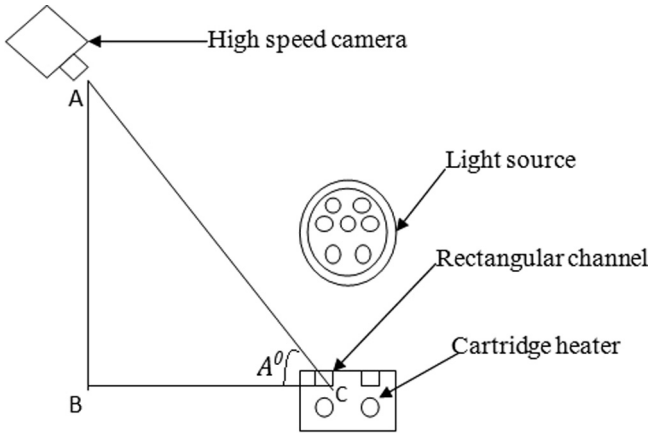

Fig. 5b. High speed camera and the channel.

Table 3
Uncertainties of measured and calculated parameters.

Parameters	Uncertainties
Thermocouple	±0.35 °C(RSS)/±0.1 °C (resolution)
Preheater temperature	±0.1 °C (resolution)
Mass flow rate	±2.32%
Mass flux	±0.77%
Heat flux	±13.3%
Heat transfer coefficient	±9.11%
Bubble departure diameter	±13.02%

$$h_{fc} = 0.023 Re^{0.8} Pr^{0.4} \frac{k_l}{D_h} \tag{8}$$

$$h_{pb} = 0.00122 \frac{k^{0.79} C_P^{0.45} \rho_l^{0.49}}{\sigma^{0.5} \mu_l^{0.29} h_{fg}^{0.24} \rho_g^{0.24}} \Delta T_{Sat}^{0.24} \Delta p_{Sat}^{0.75} \tag{9}$$

$$S = \frac{1}{1 + 2.53 \times 10^{-6} Re^{1.17}} \tag{10}$$

F is the constant which depends on the fluid used. F can be chosen as 1 of water.

Gungor and Winterton modified the Chen correlation by introducing the dependence on the boiling number (Bo) in the enhancement factor E and proposed the Cooper correlation for pool boiling heat transfer [19].

$$h_{pb} = 55 \left(\frac{P}{P_{cr}}\right)^{0.12} \left[-\log_{10}\left(\frac{P}{P_{cr}}\right)\right]^{-0.55} M^{-0.5} q''^{0.67} \tag{11}$$

$$S = \frac{1}{1 + 1.15 \times 10^{-6} E^2 Re^{1.17}} \tag{12}$$

$$E = 1 + 24000 Bo^{1.16} + 1.37 \left(\frac{1}{\chi_{tt}}\right)^{0.86} \tag{13}$$

$$\chi_{tt} = \left(\frac{1-x}{x}\right)^{0.9} \left(\frac{\rho_g}{\rho_l}\right) \left(\frac{\mu_l}{\mu_g}\right)^{0.1} \tag{14}$$

The present experiment is conducted for subcooled region; hence the Martinelli parameter can be neglected. h_{tp} and h_{fc} are calculated by Eqs. (13) and (12) respectively. Liu and Winterton [19] proposed a power-type addition model for the prediction of subcooled flow boiling heat transfer. Their experiments were carried out in tubes and annuli and covered a range of G = 12.4–8180 kg/(m^2-s), P = 0.05–20 MPa, and T_{sub} = 0–173 °C. The correlation for subcooled flow boiling heat transfer coefficient is expressed as:

$$h_{tp} = \sqrt{Fh_{fc}^2 + \left(Sh_{pb} \frac{T_{Wall} - T_{Sat}}{T_{Wall} - T_{Sat}}\right)^2} \tag{15}$$

$$S = \frac{1}{1 + 0.0055 F^{0.1} Re_l^{0.16}} \tag{16}$$

h_{pb} is calculated by Eq. (11).

Kandlikar [20] proposed subcooled boiling correlations for water and is by Eq. (22):

$$\frac{h_{tp}}{h_{fc}} = 1058 Bo^{0.7} F \tag{17}$$

h_{fc} is calculated by the Eq. (18) and the value of F depends upon the type of fluid used. For water the value can be chosen as 1.

$$Nu = 7.55 + \frac{0.024 (z^*)^{-1.14}}{1 + 0.035 Pr^{0.17} z^{*-0.64}} \tag{18}$$

For a parallel rectangular channel, Stephan correlated numerical results for Nusselt number as shown in Eq. (18). This equation is valid for Prandtl numbers varying from 0.1 to 1000 and for laminar flows. z^* is dimensionless channel length and can be assumed to be 0.5 [21]. In the present experiment the flow is maintained at laminar condition i.e., average Reynolds number 500–2500.

Fig. 6 shows the comparison of subcooled boiling heat transfer coefficient data of water with those predicted using available literature correlations. Gungour and Winterton correlation predicts the experimental data with mean absolute error (MAE) of 8.82%. Kandlikar correlation predicts the experimental data with MAE of 11.46%. Liu and Winterton correlation predicts the experimental data with MAE of 13.31%. Chen correlation under predicts the experimental data with MAE of 21.37%. The correlations predicted the values of the experimental data reasonably well. The deviation is attributed to non uniform temperature distribution in cold plate, assumption of one dimensional temperature distribution to calculate heat flux.

3.2. Bubble departure diameter

3.2.1. Size distribution of bubble departure diameter

The bubble departure diameter is one of the important parameters to understand boiling phenomenon. The bubble departure diameter is measured and its relation with heat transfer coefficient is discussed. The bubble departs from the nucleation sites. The departure diameters, growth periods and waiting period are dependent on nucleation sites [22,23]. However, only few bubbles departed from a site. Therefore average of 20–30 bubbles is considered during departure from the 3–4 sites to measure the bubble departure diameter. The size distribution of these bubbles follows the Gaussian distribution curve as shown in Fig. 7. The size distribution is given in Eq. (19).

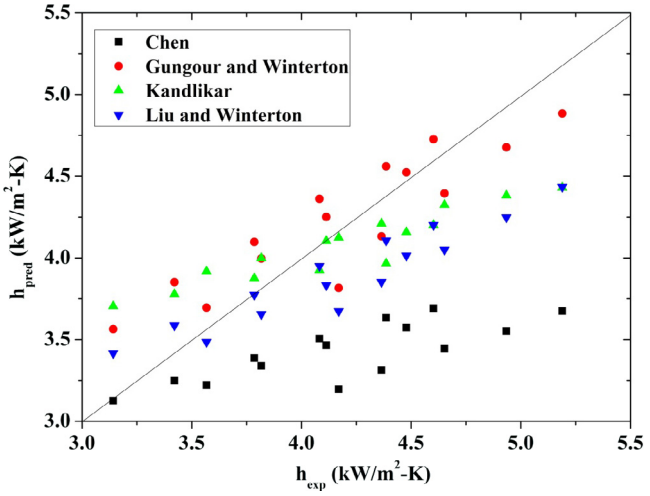

Fig. 6. Comparison of subcooled flow boiling heat transfer coefficient values of water with correlations.

$$f(size) = \frac{N(d_i)}{\sum_{i=1}^{\infty}[N(d_i)(d_{i+1} - d_i)]} \tag{19}$$

3.2.2. Validation

Despite several efforts over many years, there are only a few correlations of bubble departure diameter. Fritz [24] first derived a simple correlation for bubble departure diameter which was a balance between surface tension and buoyancy force. Few correlations were proposed with considerations of pressure, superheat and wettability effects. Cole and Rohsenow [25] correlated bubble departure diameter for various fluids at low pressure which is given by Eq. (20).

$$d_{dep} = C\sqrt{\frac{\sigma_s}{\rho(\rho_f - \rho_v)}}\left(\frac{\rho_f C_{pf} T_{Sat}}{\rho_g h_{fg}}\right)^{5/4} \tag{20}$$

A different approach to determine the bubble departure diameter has been developed by researchers based on heat transfer mechanisms. Kurul and Podowski [26] derived the correlation for bubble departure diameter by balancing the heat supplied to the wall with the heat used to grow a bubble by evaporating underlying micro layers which is represented by Eq. (21).

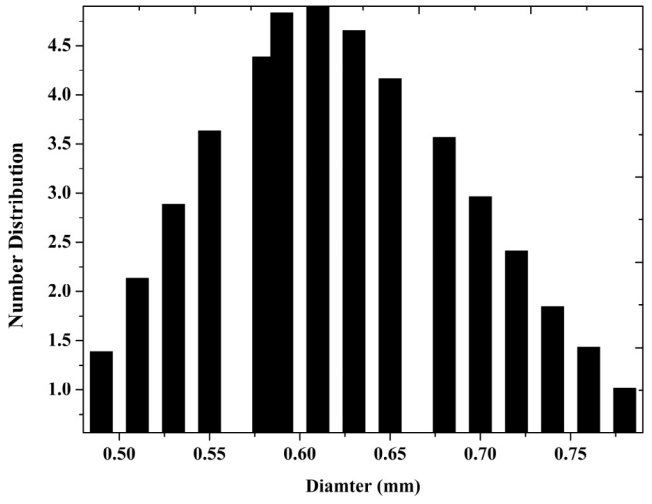

Fig. 7. Size distribution for bubble departure diameter at heat flux = 90 kW/m^2 and mass flux = 76.67 kg/m^2-s.

$$d_{dep} = 0.00014 + 10^{-4} T_{sub} \tag{21}$$

Zuber [27] included the effect of non-uniform temperature field and gave the bubble radius as represented by Eq. (22).

$$d_{dep} = \frac{4b}{\sqrt{\pi}} Ja\sqrt{\alpha_l t} \tag{22}$$

Mikic and Roshsenow [28] equations are used to nondimensionalise the bubble departure radius in the present work. These equations are applicable for both inertia controlled and diffusion controlled stages.

$$\frac{1}{A^2}\left(\frac{dr}{dt}\right)^2 + \frac{2\sqrt{t}}{B}\frac{dr}{dt} - 1 = 0 \tag{23}$$

where constant A and B are defined as,

$A = \left(\frac{b\Delta T h_{fg}\rho_V}{T_{sat}\rho_l}\right)^{0.5}$ $B = \left(\frac{12}{\pi} Ja^2 \alpha_l\right)^{0.5}$ $b = \frac{\pi}{7}$ for bubble growth on the surface of channel wall. The dimensionless bubble departure radius is given by:

$$r^+ = \frac{r_{dep}}{B^2/A} \quad \text{and} \quad d^+ = 2r^+$$

Fig. 8 shows the comparison of measured bubble departure diameter in dimensionless form with the available literature correlations. Cole-Roshnew Correlation predicts the experimental data with mean absolute error (MAE) of 31.4% and 85% of experimental data are under predicted by the correlation. Kurul-Podowski correlation under predicts the experimental data with MAE of 38.1%. Zuber correlation predicts the experimental data with MAE of 32.9% and out of which 65% of experimental data are over predicted by Zuber correlation. Cole-Roshnew correlation is based on force balance approach and Kurul-Podowski and Zuber correlations are based on heat balance approach. The force balance approach predicts the present experimental data better when compared to that of heat balance approach.

3.2.3. Effect of heat flux and mass flux

Fig. 9 shows the variation of dimensionless bubble departure diameter with mass flux at different heat flux. It is observed that the bubble radius and bubble departure radius decreases with increase in mass flux and decreases with increase in heat flux. Sugrue et al. [29] had conducted subcooled flow boiling experiment for water in a vertical channel. They found that bubble departure decreased with increase in mass flow flux and heat flux. When the bubble is formed in the active nucleation sites, it coheres at the

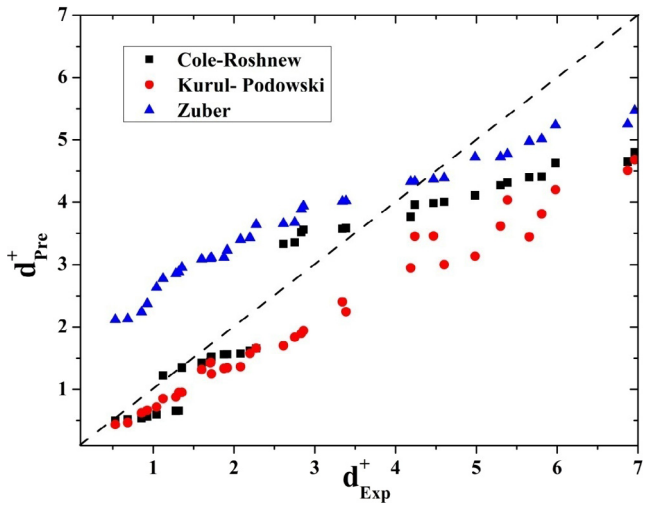

Fig. 8. Validation of bubble departure diameter in dimensionless form.

channel wall due to surface tension between the channel wall-vapour interfaces. Surface energy of channel wall tends to pull the molecules of local vapour causing wetting of the channel surface known as wettability. The wetting of surface is dependent on the contact angle between the channel wall surface (solid-vapour interface) and the bubble. When contact angle increases, the wettability decreases and bubble departs from the surface. At higher heat flux, mass flux and at lower inlet temperature of the fluid, the surface tension between the channel wall and the vapour decreases due to decrease in surface energy. The surface energy decreases at higher heat flux, mass flux and at lower inlet temperature of water because (i) Buoyancy force, inertia and pressure force increase due to increase in evaporation at higher heat flux. This pulls the bubble away from the channel wall surface and decreases the surface tension between the solid-vapour interfaces. (ii) At higher mass flux, the bulk liquid pushes the bubble downstream and this also causes to decrease in surface tension between the solid-vapour interfaces.

Surface tension in the vapour-liquid interface increases in order to overcome the loss of surface tension between channel wall-vapour interfaces. This attracts the surface of the bubble towards the liquid causing an increase in vapour-liquid interface pressure and buoyancy of the bubble. Initially, the formation of bubbles reduces the overall heat transfer due to the thin vapour layer of bubbles providing thermal resistance. But the surface tension of the vapour-liquid interface will be higher than the inertial force of the liquid and the bubbles departure at faster rate. This reduces the bubble departure diameter and thus increases the heat transfer coefficient. Departed bubble acts as an energy carrier and increases the overall heat transfer coefficient of the liquid. This phenomenon is observed at higher heat flux and higher mass flux. At higher heat flux, an increase in heat transfer coefficient increases due to early bubble departure and formation of more number of active nucleation sites, i.e. bubble formation. But at higher mass flux, the bubble departs at earlier stage, but active nucleation site formation is reduced due to decrease in wall temperature. Therefore, effect of increase in heat flux on heat transfer coefficient is more significant when compared with that of mass flux. Fig. 10 shows the variation of heat transfer coefficient with heat flux for water at different mass fluxes. It can be seen that at the subcooled boiling stage the curve almost merges when mass flux increases.

3.2.4. Effect of channel inlet temperature

Fig. 11 shows the variation of dimensionless departure diameter with mass flux at different inlet temperature. It is seen that bubble departure diameter increases with increase in inlet temperature, because at higher inlet temperature the bubbles adhere to wall due to decrease in surface tension between the liquid-vapour interfaces. Su et al. [30] conducted numerical investigation on bubble dynamics during flow boiling of water. In their research it was found that the bubble departure diameter decreased with increase in subcooling, i.e. decrease in inlet fluid temperature.

3.3. Bubble growth period and waiting period

The time period from bubble nucleation to departure is called growth period. The time period from the bubble departure to the next bubble nucleation is called waiting period. Figs. 12–15 show the photographic image of bubble growth of water at different heat flux, mass flux and inlet temperature. In the images, some of the bubbles are larger in size. They are the coalesced bubbles and are not considered for measuring the bubble departure diameter. Larger and smaller bubbles can also be observed. Hence 20–30 bubbles are identified from 3 to 4 sites to measure the average bubble departure diameter.

3.3.1. Effect of heat flux and mass flux on bubble growth period

Fig. 16 shows the variation of dimensionless bubble growth period with the mass flux for different heat flux. The dimensionless bubble growth period is obtained by dividing the bubble growth period with the total period. The total period is the sum of growth period and waiting period. It can be seen that the growth period decreases with increase in heat flux and mass flux. But the influence of heat flux is observed to be more significant than mass flux. Because at higher heat flux and mass flux sufficient amount of energy will be acquired by the fluid and overcomes intermolecular force of the molecules causing change in phase of liquid locally. This causes bubbles to depart from the surface and thus reduces the bubble growth period.

3.3.2. Effect of channel inlet temperature on bubble growth period

Variation of dimensionless bubble growth period with mass flux for various inlet temperature is shown in Fig. 17. It can be observed that the bubble growth period increases with an increase in inlet temperature. Higher inlet temperature reduces the heat transfer coefficient due to increase in thermal boundary layer thickness and thus causing an increase in growth period. At higher

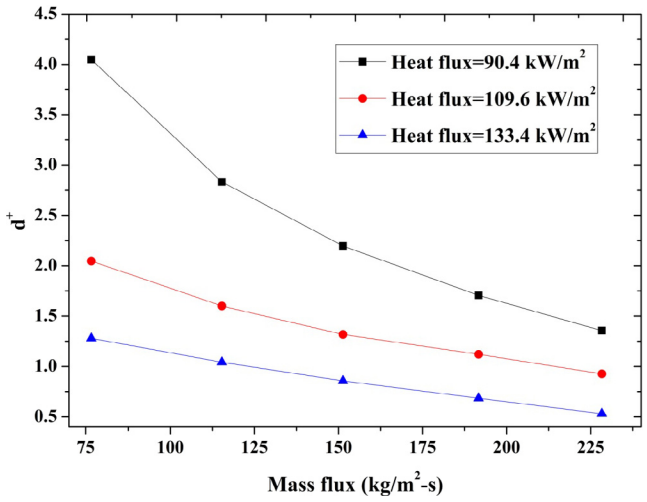

Fig. 9. Variation of dimensionless bubble departure diameter with mass flux for different heat flux at inlet water temperature of 303 K.

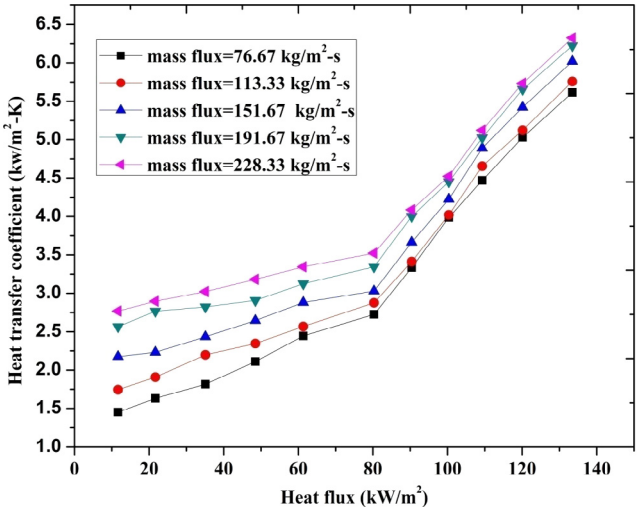

Fig. 10. Variation of heat transfer coefficient with heat flux for water at different mass flux.

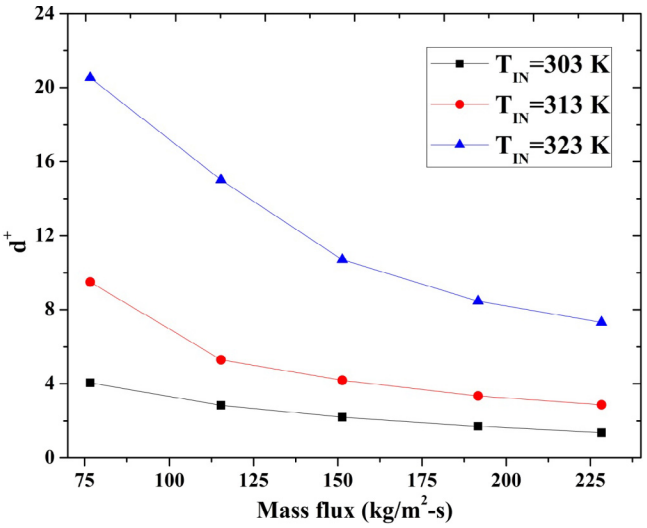

Fig. 11. Variation of dimensionless bubble departure diameter with mass flux for different inlet temperatures of water at 90.4 kW/m^2.

inlet temperature the bubbles adhere to wall because of decrease in surface tension between the liquid-vapour interfaces and thus increases the bubble growth period.

3.3.3. Relation between bubble growth period and bubble waiting period

Fig. 18 shows the variation of dimensionless bubble diameter with dimensionless growth period of bubble for different mass flux. Dimensionless bubble diameter is obtained by dividing the instantaneous bubble diameter during the growth stage to bubble departure diameter. Dimensionless growth period is obtained by dividing the instantaneous time during the growth stage to time taken for bubble to depart. The dimensionless bubble diameter increases with increase in dimensionless time. During the bubble growth period a high rate of energy is extracted from the heater surface, which leads to significant temperature drop beneath the bubble [31]. The clusters of water molecules escape as vapour in the form of bubbles at faster rate. This reduces the size of bubble due to early growth and departure.

The early bubble departure decreases the bubble growth period and bubble departure diameter size and thus increases the heat transfer coefficient. After the departure of the bubble, the molar latent heat of vapourization increases and more heat is available to break the intermolecular force of liquid in the same site and decreases the waiting period and heat transfer coefficient. Therefore the bubble growth period increases with increase in waiting period as shown in Fig. 19.

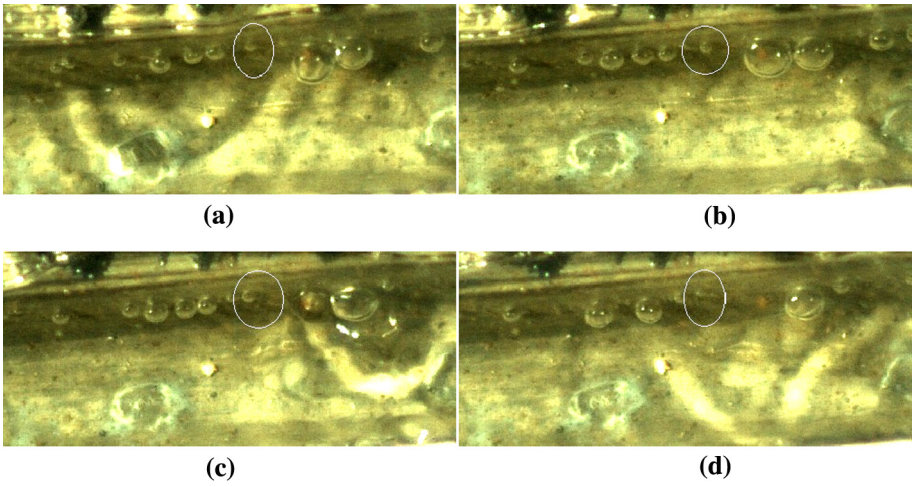

Fig. 12. Bubble growth and waiting periods for water at heat flux = 90.4 kW/m^2, inlet temperature = 303 K and mass flux of 228.3 kg/m^2-s (a) Bubble nucleation at 0 ms, (b) bubble in growth stage at 6.23 ms, (c) bubble departure at 12.45 ms, (d) next bubble nucleation after 28.9 ms after the departure.

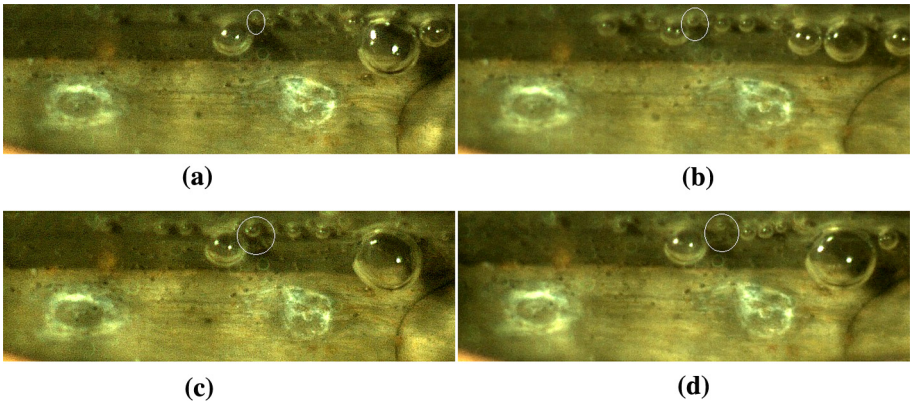

Fig. 13. Bubble growth and waiting periods for water at heat flux = 133.47 kW/m^2, inlet temperature = 303 K and mass flux of 76.67 kg/m^2-s (a) Bubble nucleation at 0 ms, (b) bubble in growth stage at 3.24 ms, (c) bubble departure at 6.48 ms, (d) next bubble nucleation after 18.54 ms after the departure.

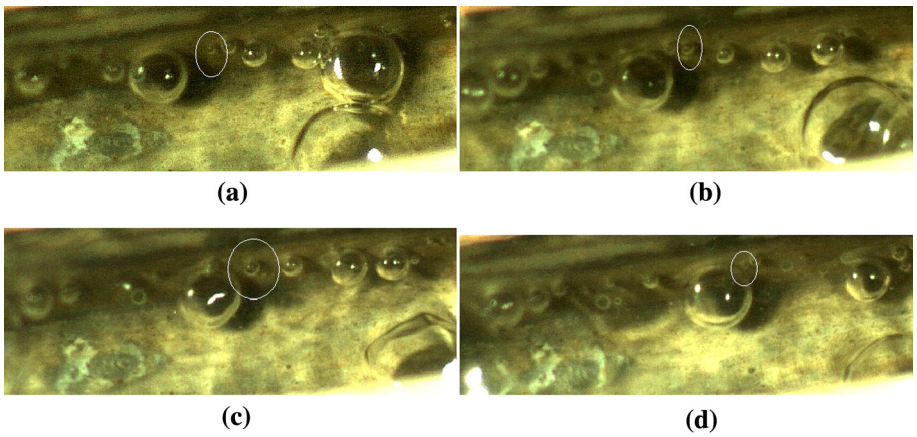

Fig. 14. Bubble growth and waiting periods for water at heat flux = 133.47 kW/m^2, inlet temperature = 303 K and mass flux of 228.33 kg/m^2-s (a) Bubble nucleation at 0 ms, (b) bubble in growth stage at 2.39 ms, (c) bubble departure at 4.78 ms, (d) next bubble nucleation after 13.97 ms after the departure.

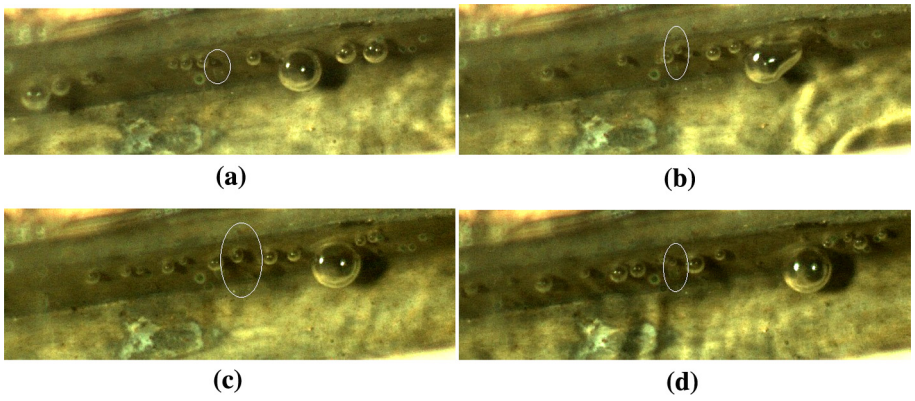

Fig. 15. Bubble growth and waiting period for water at heat flux = 133.47 kW/m^2, inlet temperature = 313 K and mass flux of 76.67 kg/m^2-s (a) Bubble nucleation at 0 ms, (b) bubble in growth stage at 5.45 ms, (c) bubble departure at 10.89 ms, (d) next bubble nucleation after 26.57 ms after the departure.

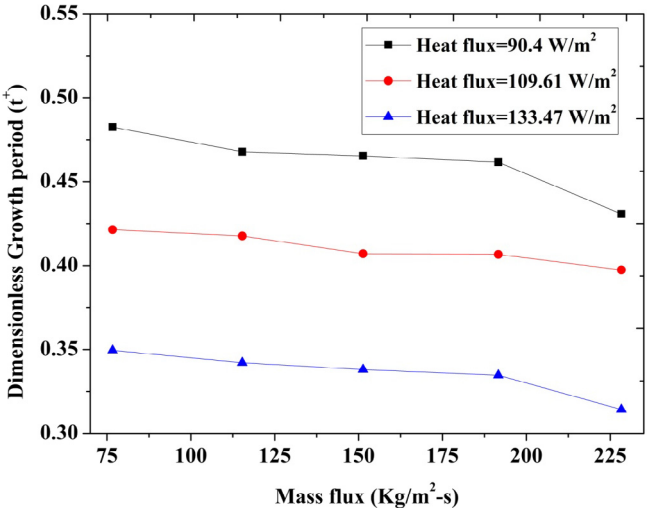

Fig. 16. Variation of dimensionless bubble growth period of water with mass flux for different heat fluxes.

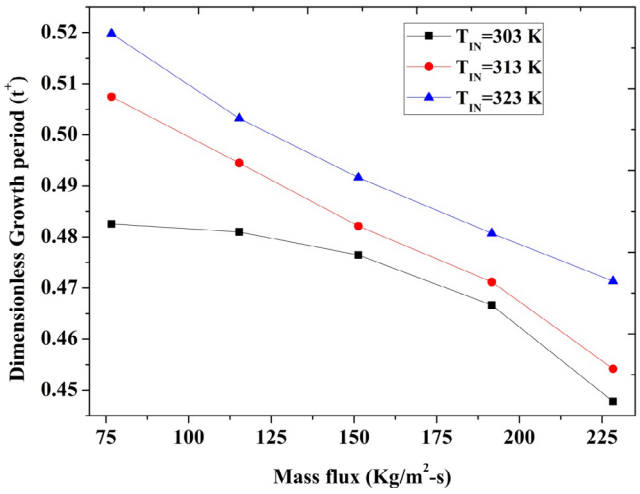

Fig. 17. Variation of dimensionless bubble growth period of water with mass flux for different inlet temperature.

3.4. Proposed correlation

A new empirical correlation for the heat transfer coefficient of pure water based on parameters like heat flux, bubble departure diameter, waiting period and growth period is developed. The proposed new empirical correlation is given by Eq. (24). The empirical correlation is applicable at heat flux varying from 90.4 kW/m^2 to 133.47 kW/m^2, mass flux varying from 76.67 kg/m^2-k to 228.33 kg/m^2-K, inlet temperature varying from 303 K to 323 K.

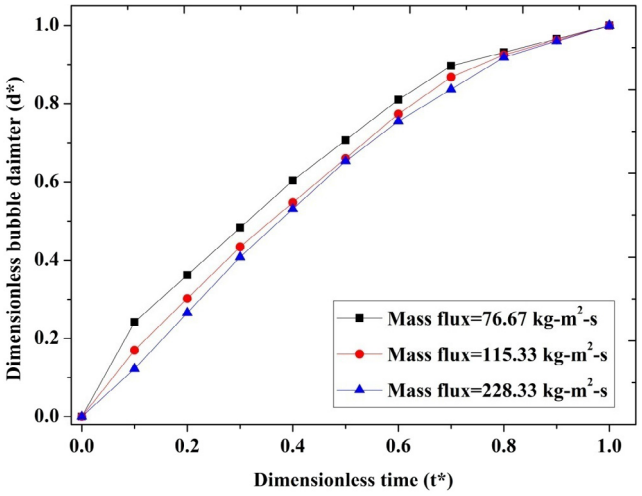

Fig. 18. Variation of dimensionless bubble departure diameter with dimensionless time for water.

$$h = \frac{4.298 q''^{0.377}}{d_{dep}^{0.178} t_g^{0.09} t_w^{0.148}} \quad (24)$$

The present empirical correlation is validated with the experimental values of heat transfer coefficient. The correlation under predicts the experimental data with MAE of 22.47% as shown in Fig. 20.

3.5. Effect of ethanol volume fraction on bubble departure diameter

The variation of dimensionless bubble departure diameter with ethanol volume fraction is shown in Fig. 21. The bubble departure diameter and growth period is highest for mixture with 75% ethanol volume fraction and lowest for mixture with 25% ethanol volume fraction. This is the reason for highest values of heat transfer coefficient for mixture with 25% ethanol volume fraction and lowest for mixture with 75% ethanol volume fraction as shown in Fig. 22. The thermal conductivity and thermal capacity of ethanol is lower than that of water. Molar entropy of vapourization of ethanol is marginally above water. The entropy is due to the molecules that are held together in liquid by polar attractions and hydrogen bonding. Hence more energy is required to pull these molecules

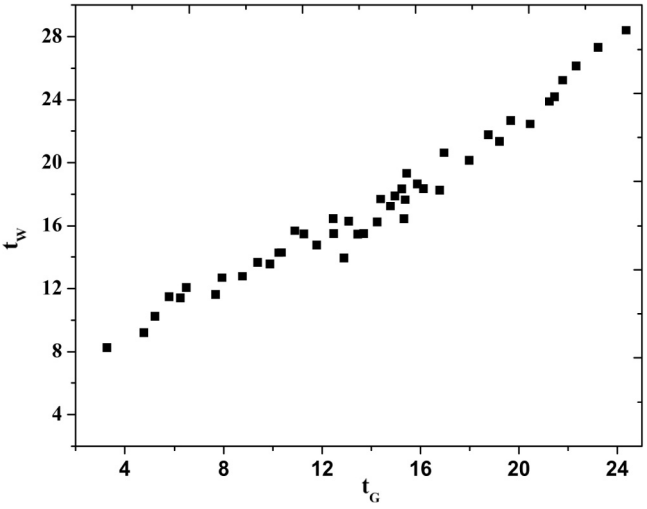

Fig. 19. Variation of waiting period of bubbles with growth period of bubbles for water.

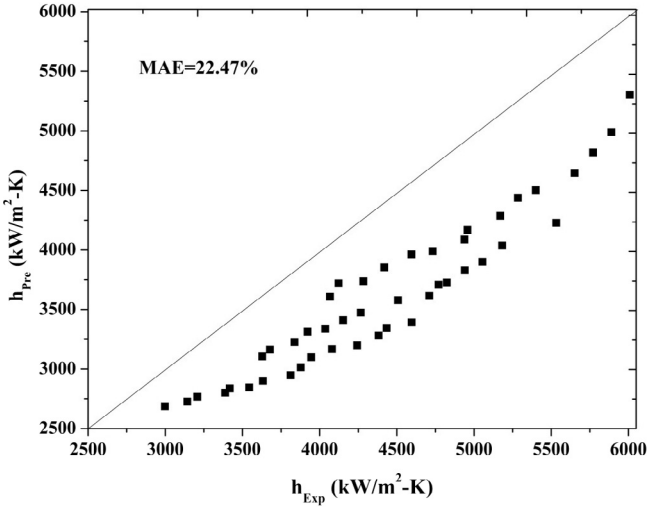

Fig. 20. Variation of predicted values of heat transfer coefficient with the experimental values of heat transfer coefficient.

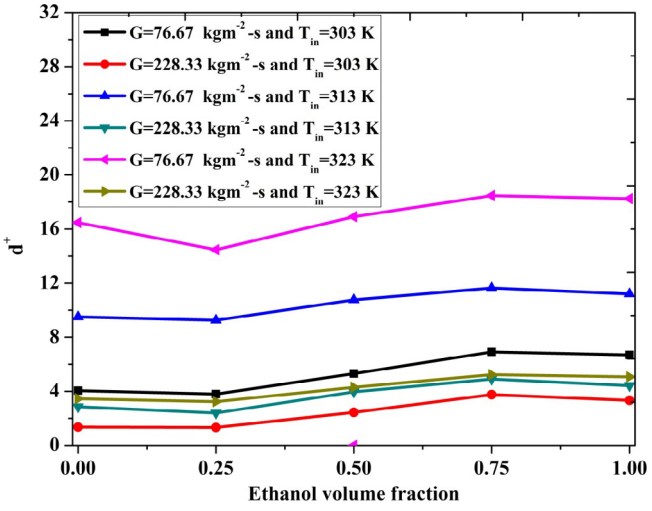

Fig. 21. Variation of bubble departure diameter with ethanol volume fraction.

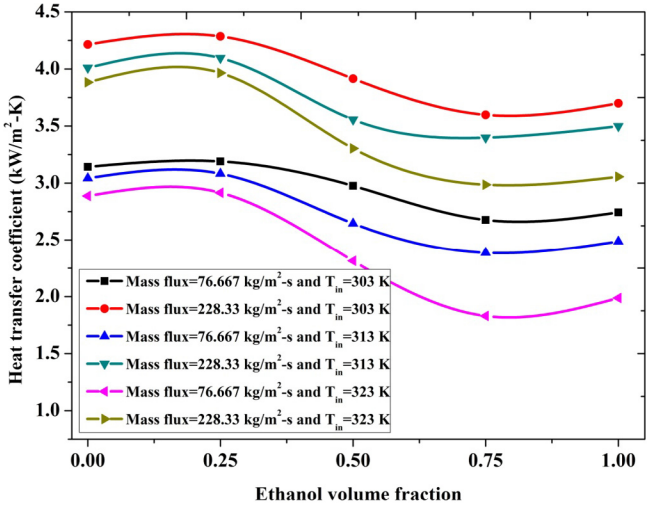

Fig. 22. Variation of heat transfer coefficient with mixture of ethanol volume fraction.

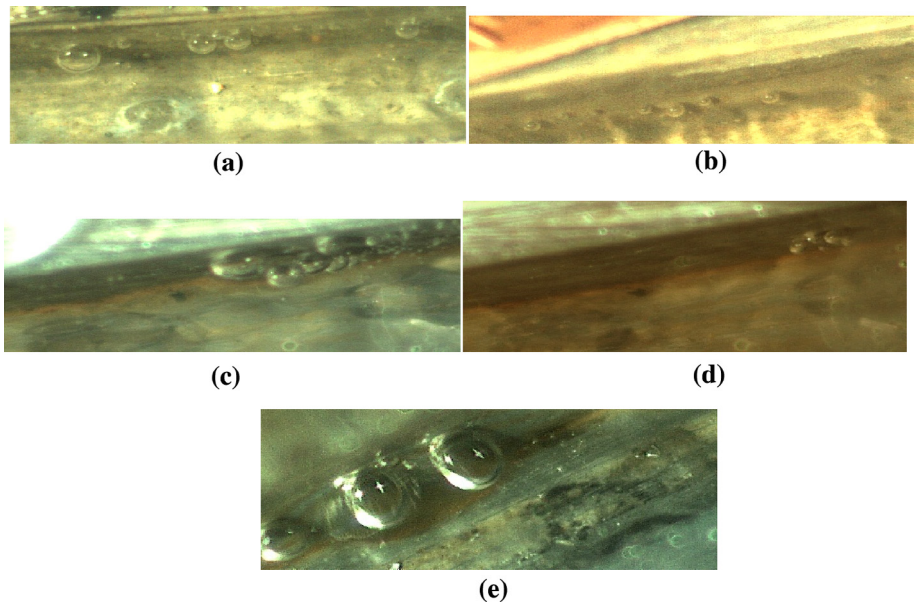

Fig. 23. Bubble formation for at heat flux = 90.4 kW/m^2, inlet temperature = 303 K and mass flux = 76.67 kW/m^2. (a) Water, (b) 25% ethanol volume fraction, (c) 50% ethanol volume fraction, (d) 75% ethanol volume fraction, (e) ethanol.

of liquid. The molar latent heat of vapourization is slightly greater which actually results in higher heat transfer coefficient of ethanol [32]. But Trouton's rule states that due to lower boiling point of ethanol, it has lower molar enthalpy of vapourization when compared with that of water [33]. Hence the addition of ethanol to water delays the departure of bubbles, thus decreasing the heat transfer coefficient from the site causing an increase in bubble departure diameter. Delay in departure increases the time gap between departure of first bubble and nucleation of next bubble resulting in decrease of active nucleation sites. But in contrast the active nucleation sites are highest for 25% and lowest for 75% ethanol volume fraction as shown in Fig. 23(a)–(e). The reason for such phenomena can be explained by force balance approach. During bubble departure for mixture with 25% ethanol volume fraction the surface tension force dominates the force developed due to unsteady bubble growth and quasi-static drag force which are parallel to flow direction. The surface tension force between the liquid-vapour interface is larger when compared to other volume fractions. This leads to earlier departure of the bubble. Early departure leads to decrease in bubble departure diameter size and thus increases the bubble formation and heat transfer coefficient. The mixture has lower heat transfer coefficient than that of pure component is due to presence of local vapour of the lower boiling component in the mixture [34]. Therefore, the ethanol is having higher heat transfer coefficient and lower departure diameter than that of mixture with 75% ethanol volume fraction as shown in Figs. 21 and 22.

3.6. Force balance approach

Klausner et al. [35] and Zeng et al. [36] conducted studies on force balance approach. They concluded that during flow, the influence of various forces acting on a bubble caused bubble departure and bubble lift-off. In the present work, their approach is used to calculate various forces acting on the bubble. The forces acting on the bubble in the parallel and normal directions to flow are:

$$\sum F_x = F_{sx} + F_{qs} + F_{du}\sin\theta \tag{25}$$

$$\sum F_y = F_{sy} + F_{sL} + F_b + F_h + F_{cp} + F_{du}\cos\theta \tag{26}$$

Force balance in parallel direction (F_x):

$$F_{sx} = -1.25 d_{dep}\sigma_s \frac{\pi(\alpha_a - \beta_r)}{\pi^2 - (\alpha_a - \beta_r)^2} \tag{27}$$

α_a and β_r are advancing and receding angles. These angles can be estimated through $\alpha_a = \theta + 10$ and $\beta_r = \theta - 10$ [37].

$$F_{qs} = \frac{1}{2} C_D \rho_L \Delta V^2 r_{dep}^2 \tag{28}$$

C_D is drag coefficient and is determined by Ishii and Zuber correlation [38].

$$C_D = \frac{2}{3}\left(\frac{g(\rho_l - \rho_g)}{\sigma_s}\right)^{0.5} \tag{29}$$

$$F_{du} = -\rho_l \pi r_{dep}^2 \left(\frac{3}{2} C_s \frac{dr}{dt} + r_{dep}\frac{d^2 r}{dt^2}\right) \tag{30}$$

where r_{dep} is the bubble departure radius, ΔV is the relative velocity between the bubble and flowing liquid. In the present work, the average of 30 sliding bubbles is noted down with respect to time. The pixels/frames are converted into velocity (metre per second). The bubbles included are (i) departed and sliding and (ii) departed, sliding and lift-off bubbles.

Force balance in normal direction (F_y):

$$F_{sy} = -d_{dep}\sigma_s \frac{\pi}{\alpha - \beta}(\cos\beta_r - \cos\alpha_a) \tag{31}$$

The dynamic actions on the vapour-liquid interface within the quasi-static regime permit the application of the Young-Laplace equation for a departing bubble yielding upward force due to contact pressure [39] as given by the Eq. (32).

$$F_{cp} = \frac{\pi d_{dep}^2}{4}\frac{2\sigma}{r_r} \tag{32}$$

r_r is radius of curvature of the bubble at the Ref. point on the surface, i.e., radius of curvature at the base of the bubble. The radius of curvature is considered as $r_r = 5\ r_{dep}$ [40]. The radius that is in contact with the surface quantifies capillary force.

$$F_b = \frac{4}{3}\pi r_{dep}^3(\rho_l - \rho_g)g \tag{33}$$

Spherical bubble assumption is used for the calculation of force due to buoyancy. It is well known that this is an approximation since the contact with the surface truncates the bubble [41].

$$F_h = \frac{9}{8}\rho_l \Delta v^2 \frac{\pi d_{dep}^2}{4} \tag{34}$$

$$F_{sl} = \frac{1}{2} C_L \rho_L \Delta V^2 r_{dep}^2 \tag{35}$$

where $C_L = 0.8\ Gs$.

$$Gs = \frac{dv}{dy}\frac{r_d}{\Delta v} \tag{36}$$

Gs is the dimensionless shear rate given by the gradient dv/dy. It can be calculated from the universal velocity profile for turbulent flow which is given by Eq. (37).

$$\frac{v}{u_\tau} = 2.5 ln y^+ + 2.5 \tag{37}$$

The velocity profile in Eq. (37) is assumed to be the time averaged velocity distribution at channel surface of the wall. y^+ in the present experiment is found to be more than 30, which lies in the logarithmic layer. The friction velocities are then substituted in Eq. (24) to find the gradient dv/dy.

The growth of a bubble is influenced by forces acting in parallel and normal directions to the horizontal heating surface. For horizontal subcooled flow boiling, forces acting on the bubble in the parallel direction influence the bubble sliding on the heated wall, whereas, the forces acting in the normal direction causes the bubble lift-off. The force balance can be studied by Jakob number which is the ratio of sensible heat absorbed to latent heat transfer. The sensible heat transfer is related to forced convection and latent heat is related to heat transfer during phase change. During subcooled flow boiling the forced convection is dominated by evaporation and agitation. Hence higher heat transfer coefficient during subcooled flow boiling has lower Jakob number. Fig. 24 shows the variation of $(F_y - F_x)$ with Jakob number. It is seen that at Jakob number lower than 20 the difference between $(F_y - F_x)$ is negative and at Jakob number above 20 the difference between $(F_y - F_x)$ is positive. When the difference is positive it is observed that bubble departed and lifted off from the heated surface of channel wall but did not slid. When the difference is negative it is observed that the bubble departed from the surface of the channel wall and also slid along the heated surface. But some of the bubbles lifted-off after sliding for small distance. This is similar to the result obtained in the literature [42].

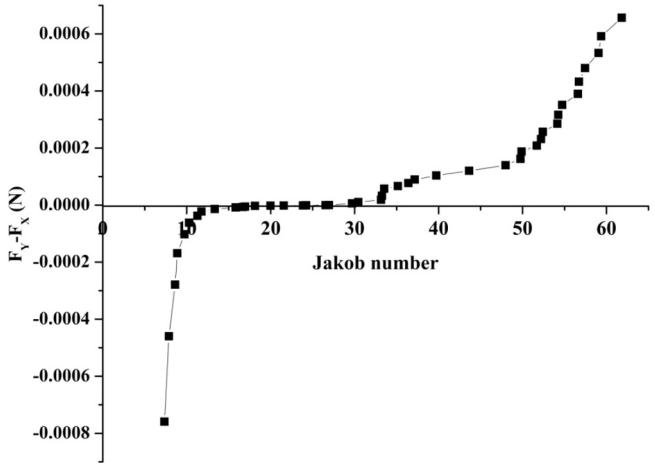

Fig. 24. Variation of $(F_Y - F_X)$ with Jakob number.

The bubble causes the change in the flow field which resulted in the variation of quasi-steady drag force (F_{qd}) and surface tension force acting on it. These forces are balanced by unsteady growth rate (F_{du}). Due to the initial immobility and the very small growth rate of the bubble in subcooled liquid, change in F_{qs} is not much significant. The breaking of the force balance in flow direction is caused by the sudden variation of the surface tension force between the wall and the liquid interface. The bubble contact diameter and the contact angles change due to the evaporation in the triple-phase line region at the bubble root during bubble growth. The force balance in flow direction is broken by the disturbance from the main flow which alters the contact diameter and the contact angles, leading to the change of the surface tension force [43]. This is achieved at higher mass flux and therefore the bubble departs earlier at higher mass flux.

The bubble begins to slide along the heated wall. Even though the force balance acting on the bubble in flow direction suddenly brakes, it could recover soon due to the adaptive surface tension force caused by the flexibility of the bubble-liquid interface which causes the bubble to slide. The bubble lift-off after departure without sliding does not cause significant increase in heat transfer because the bubble gets condensed into the subcooled liquid in the outer region of boundary layer. But during sliding the bubble movement causes the micro layer evaporation beneath the bubble and carries as energy carrier. This increases the temperature gradient beneath the bubble to cause an increase in heat transfer. During bubble lift-off the sum of hydrodynamic pressure and surface tension force will be lower than contact pressure force, shear lift force, unsteady growth force and buoyancy force [44].

The Jakob number increases with increase in volume fraction. The heat transfer coefficient should have reduced with increase in Jakob number, but in contrast, for mixture with 25% ethanol volume fraction bubble sliding is observed for slightly higher Jakob number when compared to water. Thus marginal increase in heat transfer coefficient is observed at this mixture composition. However, the bubble lift-off occurred without sliding for 75% ethanol volume fraction and ethanol for all mass fluxes.

3.7. Hydrodynamic instability

Flow instabilities are undesirable in flow boiling. Flow oscillations affect the local heat transfer coefficient. The two kinds of flow instabilities which are identified in subcooled flow boiling are nucleation instability and oscillatory instability.

3.7.1. Nucleation instability

The nucleation instability is caused by vapourization of the local liquid which results in increase in the specific volume of the local liquid. The finite amount of wall superheat is required to initiate bubble nucleation at the heated surface. Under this condition, the bubbles grow and eject into the subcooled portion of the flow. This process will cool the remaining liquid and the heated surface of channel wall, until the required degree of super heat is reestablished for further nucleation. It depends mainly on the geometry of the system and fluid properties. Therefore it may be observed that nucleation instability increases at higher ethanol volume fraction resulting in obtaining lower heat transfer coefficient.

3.7.2. Oscillatory instability

When a bubble is formed and departed from the heated surface, disturbance occurs in the flow. In the mixture, ethanol which is the higher volatile component evaporates earlier. Bubble formed due to evaporation of this volatile component compresses the sur-

rounding liquid while growing and leaves the wall surface. The incoming flow is driven to the compressible volume from the bubble which has departed. The inertia of the flow from the compressible volume will cause reduction in local pressure at the heated inlet of the channel. This causes to and fro motion in the channel surface leading to the compression of vapour boundary layer. The rarefaction wave also passes through the surface, thus expanding and decreasing the thermal boundary layer. Usually, this phenomenon is observed at higher volume fractions and higher inlet temperatures.

4. Conclusions

Bubble dynamics in water ethanol mixture subcooled flow boiling is investigated through visualization using a high speed camera for various experimental parameters like heat flux, mass flux, fluid inlet temperature and ethanol volume fraction. Following are the conclusions drawn from the present experiment.

- The two types of bubble behaviour observed after nucleation were: (1) Lift-off from the bottom wall of the channel surface followed by rapid collapse in subcooled bulk liquid at lower heat flux, and at addition of higher ethanol volume fraction. (2) Sliding along the bottom wall of the channel surface for a distance and lifting off from the channel wall surface. These are observed at higher heat flux for water. The effect of mass flux on the bubbles sliding or bubble lift-off are not significant.
- The bubble growth period increases with decrease in heat flux and mass flux. It also increases with increase in channel inlet temperature. The bubble growth period increases with increase in waiting period.
- The bubble departure diameter should have increased with increase in ethanol addition. But the size of the bubble departure diameter is highest for mixture with 75% ethanol volume fraction and smallest for mixture with 25% ethanol volume fraction.
- At 25% volume fraction the bubble slides for longer distance and lifts off when compared to pure water.
- The bubble lift-off is highest for mixture with 75% ethanol volume fraction and pure ethanol. The bubbles lifted-off without sliding for this mixture and pure ethanol.
- During subcooled flow boiling the forced convection is dominated by evaporation and agitation. Hence the higher heat transfer coefficient has the lower Jakob number. It is seen that at Jakob number lesser than 20 the difference between $(F_y - F_x)$ is negative and above 20 the difference between $(F_y - F_x)$ is positive.
- The nucleation and oscillatory instabilities is observed during the flow at higher ethanol volume fraction addition.

Acknowledgment

The authors acknowledge the contribution of center for system design: A center of Excellence at NITK Surathkal pertaining to issuance of LAB view software. The technical support received from the members of SOLVE: The virtual lab at NITK Surathkal is deeply appreciated.

References

[1] K. Sefiane, D. Sefiane, G. Duursma, A.J. Walton, Bubble dynamics and flow boiling instabilities in microchannels, Int. J. Heat Mass Transfer 58 (2013) 663–675.
[2] M.S. Plesset, S.A. Zwick, The growth of vapor bubbles in superheated liquids, J. Appl. Phys. 25 (4) (1954) 493–500.
[3] H.K. Forster, N. Zuber, Growth of a vapor bubble in a superheated liquid, J. Appl. Phys. 25 (4) (1954) 474.
[4] B.B. Mikic, W.M. Rohsenow, P. Griffith, On bubble growth rates, Int. J. Heat Mass Transfer 13 (1970) 657–666.
[5] G. Sateesh, S.K. Das, A.R. Balakrishnan, Analysis of pool boiling heat transfer: effect of bubbles sliding on the heating surface, Int. J. Heat Mass Transfer 48 (8) (2005) 1543–1553.
[6] S.G. Kandlikar, V.R. Mizo, C.D. Cartwright, E. Ikenze, Bubble nucleation and growth characteristics in subcooled flow boiling of water, HTD-Vol. 342, ASME Proc. 32nd National Heat Transfer Conf. 4 (1997) 11–18.
[7] F.C. Gunther, Photographic study of surface-boiling heat transfer to water with force convection, J. Heat Transfer 73 (1951) 115–123.
[8] N. Basu, G.R. Warrier, V.K. Dhir, Onset of nucleate boiling and active nucleation site density during subcooled flow boiling, J. Heat Transfer 124 (2002) 717–728.
[9] E.L. Bibeau, M. Salcudean, A study of bubble ebullition in forced-convective subcooled nucleate boiling at low pressures, Int. J. Heat Mass Transfer 37 (1994) 2245–2259.
[10] O. Zeitoun, M. Shoukri, Bubble behavior and mean diameter in subcooled flow boiling, J. Heat Transfer 118 (1996) 110–116.
[11] T. Okawa, T. Ishida, I. Kataoka, M. Mori, Bubble rise characteristics after the departure from a nucleation site in vertical up flow boiling of subcooled water, Nucl. Eng. Des. 235 (2005) 1149–1161.
[12] G.E. Thorncroft, J.F. Klausner, R. Mei, An experimental investigation of bubble growth and detachment in vertical upflow and downflow boiling, Int. J. Heat Mass Transfer 41 (1998) 3857–3871.
[13] Vijay K. Dhir, Hari S. Abarajith, Ding Li, Bubble dynamics and heat transfer during pool and flow boiling, Heat Transfer Eng. 28 (2007) 608–624.
[14] D. Gorenflo, V. Knabe, V. Beiling, Bubble density on surfaces with nucleate boiling—its influence on heat transfer, Proc. 8th International Heat Transfer Conference, San Francisco 4 (1986) 1995–2000.
[15] R.A.M. Al-Hayes, R.H.S. Winterton, Bubble diameter on detachment in flowing liquids, Int. J. Heat Mass Transfer 24 (1981) 223–230.
[16] J.F. Klausner, R. Mei, D.M. Bernhard, L.Z. Zeng, Vapor bubble departure in forced convection boiling, Int. J. Heat Mass Transfer 36 (1993) 651–662.
[17] S.J. Kline, F.A. McClintock, Describing uncertainties in single-sample experiments, Mech. Eng. 75 (1953) (1953) 3–8.
[18] Claudi Martin Callizo, Flow boiling heat transfer in single channel vertical diameter of small diameter, in: Department of Energy Technology, Royal Institute of Technology, Stockholm, Sweden, 2010, pp. 47–49, Doctoral Thesis.
[19] Z. Liu, R.H.S. Winterton, A general correlation for saturated and subcooled flow boiling in tubes and annuli, based on a nucleate pool boiling equation, Int. J. Heat Mass Transf. 34 (1991) 2759–2766.
[20] S.G. Kandlikar, Heat Transfer characteristics in partial boiling, fully developed boiling, Int. J. Heat Mass Transf. 120 (1998) 395–401.
[21] Chein-Hsiun Tu, Hung-Sheng Lai, Yi-Feng Lin, Isobaric (vapor + liquid) equilibria for the ternary system of (ethanol + water + 1,3-propanediol) and three constituent binary systems at P = 101.3 kPa, J. Chem. Thermodyn. 68 (2014) 13–19.
[22] Frederic J. Lesage, James S. Cotton, A.J. Robinson, Analysis of quasi-static vapours bubble shape during growth and departure, Phys. Fluids 25 (6) (1994) 067103.
[23] Frederic J. Lesage, James S. Cotton, A.J. Robinson, , A mathematical model for predicting bubble growth for low Bond and Jakob number nucleate boiling, Chem. Eng. Sci. 112 (2014) 35–46.
[24] Nilanjana Basu, Gopinath R. Warrier, Vijay K. Dhir, Onset of nucleate boiling and active nucleation site density during subcooled flow boiling, J. Heat Transfer 124 (2002) 717–728.
[25] R. Cole, W. Rohsenow, Correlation of Bubble Departure Diameters for Boiling of Saturated Liquids, AIChE Chemical Engineering Progress Symposium 65 (1969) 211–220.
[26] N. Kurul, M.Z. Podowski, Multi-dimensional effects in forced convection subcooled boiling. Proceedings of the nineth Heat Transfer conference, Jerusalem, Isreal, Hemisphere Publishing Corporation, 2 (1990), 21–26.
[27] N. Zuber, The dynamics of vapour bubbles in non-uniform temperature fields, Int. J. Heat Mass Transf. 2 (1961) 83–98.
[28] B.B. Mikic, W.M. Roshsenow, A new correlation of pool boiling data including effect of heating surface characteristics, J. Heat Transfer 91 (1969) 245–250.
[29] R. Sugrue, J. Buongiorno, T. McKrell, An experimental study of bubble departure diameter in subcooled flow boiling including the effects of orientation angle, subcooling, mass flux, heat flux, and pressure, Nucl. Eng. Des. 279 (2014) 182–188.
[30] G.H. Su, Ronghua Chen, Wenxi Tian, Suizheng Qiu, Yuki Ishiwatari, Yoshiaki Oka, Numerical investigation on bubble dynamics during flow boiling using moving particle semi-implicit method, Nucl. Eng. Des. 240 (2010) 3830–3840.
[31] B.R. Fu, M.S. Tsou, Chin Pan, Boiling heat transfer and critical heat flux of ethanol–water mixtures flowing through a diverging microchannel with artificial cavities, Int. J. Heat Mass Transfer 55 (2012) 1807–1814.
[32] James A. Green, Sheeba Jem Irudayam, Richard H. Henchman, Molecular interpretation of Trouton's and Hildebrand's rules for the entropy of vaporization of a liquid, J. Chem. Thermodyn. 43 (2011) 868–872.
[33] J. Lyklema, The surface tension of pure liquids thermodynamic components and corresponding states, Colloids Surf., Physicochem. Eng. Aspects 156 (1999) 413–421.

[34] S.G. Kandlikar, Boiling heat transfer with binary mixture: Part-II, A theoretical modeling for pool boiling, National Heat transfer conference, Baltimore, Maryland, (1998) August 8–12.
[35] J.F. Klausner, R. Mei, D.M. Bernhard, L.Z. Zeng, Vapor bubble departure in forced convection boiling, Int. J. Heat Mass Transfer 36 (1993) 651–662.
[36] L.Z. Zeng, J.F. Klausner, D.M. Bernhard, R. Mei, A unified model for the prediction of bubble detachment diameters in boiling systems. II. Flow boiling, Int. J. Heat Mass Transfer 36 (1993) 2271–2279.
[37] G.H. Yeoh, J.Y. Tu, A unified model considering force balances for departing vapour bubbles and population balance in subcooled boiling flow, Nucl. Eng. Des. 235 (2005) 1251–1265.
[38] M. Ishii, N. Zuber, Drag coefficient and relative velocity in bubbly, droplet and particulate flows, AIChE J. 25 (1979) 843–855.
[39] Frederic J. Lesage, James S. Cotton, Anthony J. Robinson, Modeling of quasi-static adiabatic bubble formation, growth and detachment for low Bond numbers, Chem. Eng. Sci. 104 (2013) 742–754.
[40] G.H. Yeoh, J.Y. Tu, A unified model considering force balances for departing vapour bubbles and population balance in subcooled boiling flow, Nucl. Eng. Des. 235 (2005) 1251–1265.
[41] Frederic J. Lesage, Francis Marois, Experimental and numerical analysis of quasi-static bubble size and shape characteristics at detachment, Int. J. Heat Mass Transfer 64 (2013) 53–69.
[42] Tomio Okawa, Rouhollah Ahmadi, Tatsuya Ueno, Bubble dynamics at boiling incipience in subcooled upward flow boiling, Int. J. Heat Mass Transfer 55 (2012) 488–497.
[43] Satish G. Kandlikar, Mark E. Steinke, Contact angles and interface behavior during rapid evaporation of liquid on a heated surface, Int J Heat Mass Transfer 45 (2002) 3771–3780.
[44] Liaofei Yin, Li Jia, Mingchen Xu, Experimental investigation on bubble sliding during subcooled flow boiling in microchannel, Exp. Therm. Fluid Sci. 68 (2015) 435–441.